

BICEP2/KECK ARRAY V: MEASUREMENTS OF *B*-MODE POLARIZATION AT DEGREE ANGULAR SCALES AND 150 GHz BY THE KECK ARRAY

P. A. R. ADE¹, Z. AHMED², R. W. AIKIN³, K. D. ALEXANDER⁴, D. BARKATS⁵, S. J. BENTON⁶, C. A. BISCHOFF⁴, J. J. BOCK^{3,7}, J. A. BREVIK³, I. BUDER⁴, E. BULLOCK⁸, V. BUZA⁴, J. CONNORS⁴, B. P. CRILL^{3,7}, C. D. DOWELL⁷, C. DVORKIN⁴, L. DUBAND⁹, J. P. FILIPPINI^{3,10}, S. FLIESCHER¹¹, S. R. GOLWALA³, M. HALPERN¹², S. HARRISON⁴, M. HASSELFIELD¹², S. R. HILDEBRANDT^{3,7}, G. C. HILTON¹³, V. V. HRISTOV³, H. HUI³, K. D. IRWIN^{2,13,14}, K. S. KARKARE⁴, J. P. KAUFMAN¹⁵, B. G. KEATING¹⁵, S. KEFELI³, S. A. KERNASOVSKIY², J. M. KOVAC⁴, C. L. KUO^{2,14}, E. M. LEITCH^{16,17}, M. LUEKER³, P. MASON³, K. G. MEGERIAN⁷, C. B. NETTERFIELD^{6,18}, H. T. NGUYEN⁷, R. O'BRIENT⁷, R. W. OGBURN IV^{2,14}, A. ORLANDO¹⁵, C. PRYKE^{8,11}, C. D. REINTSEMA¹³, S. RICHTER⁴, R. SCHWARZ¹¹, C. D. SHEEHY^{16,17}, Z. K. STANISZEWSKI^{3,7}, R. V. SUDIWALA¹, G. P. TEPLY³, K. L. THOMPSON², J. E. TOLAN², A. D. TURNER⁷, A. G. VIEREGG^{16,17}, A. C. WEBER⁷, J. WILLMERT¹¹, C. L. WONG⁴, AND K. W. YOON^{2,14}

(KECK ARRAY AND BICEP2 COLLABORATIONS)

¹ School of Physics and Astronomy, Cardiff University, Cardiff, CF24 3AA, UK

² Department of Physics, Stanford University, Stanford, CA 94305, USA; ssstokes@stanford.edu

³ Department of Physics, California Institute of Technology, Pasadena, CA 91125, USA

⁴ Harvard-Smithsonian Center for Astrophysics, 60 Garden Street MS 42, Cambridge, MA 02138, USA

⁵ Joint ALMA Observatory, ESO, Santiago, Chile

⁶ Department of Physics, University of Toronto, Toronto, ON, Canada

⁷ Jet Propulsion Laboratory, Pasadena, CA 91109, USA

⁸ Minnesota Institute for Astrophysics, University of Minnesota, Minneapolis, MN 55455, USA

⁹ SBT, Commissariat à l'Energie Atomique, Grenoble, France

¹⁰ Department of Physics, University of Illinois at Urbana-Champaign, Urbana, IL 61820, USA

¹¹ Department of Physics, University of Minnesota, Minneapolis, MN 55455, USA

¹² Department of Physics and Astronomy, University of British Columbia, Vancouver, BC, Canada

¹³ National Institute of Standards and Technology, Boulder, CO 80305, USA

¹⁴ Kavli Institute for Particle Astrophysics and Cosmology, SLAC National Accelerator Laboratory, 2575 Sand Hill Rd, Menlo Park, CA 94025, USA

¹⁵ Department of Physics, University of California at San Diego, La Jolla, CA 92093, USA

¹⁶ Kavli Institute for Cosmological Physics, University of Chicago, Chicago, IL 60637, USA

¹⁷ Department of Physics, Enrico Fermi Institute, University of Chicago, Chicago, IL 60637, USA

¹⁸ Canadian Institute for Advanced Research, Toronto, ON, Canada

Received 2015 February 3; accepted 2015 August 28; published 2015 September 29

ABSTRACT

The Keck Array is a system of cosmic microwave background polarimeters, each similar to the BICEP2 experiment. In this paper we report results from the 2012 to 2013 observing seasons, during which the Keck Array consisted of five receivers all operating in the same (150 GHz) frequency band and observing field as BICEP2. We again find an excess of *B*-mode power over the lensed- Λ CDM expectation of $>5\sigma$ in the range $30 < \ell < 150$ and confirm that this is not due to systematics using jackknife tests and simulations based on detailed calibration measurements. In map difference and spectral difference tests these new data are shown to be consistent with BICEP2. Finally, we combine the maps from the two experiments to produce final *Q* and *U* maps which have a depth of 57 nK deg (3.4 μ K arcmin) over an effective area of 400 deg² for an equivalent survey weight of 250,000 μ K⁻². The final *BB* band powers have noise uncertainty a factor of 2.3 times better than the previous results, and a significance of detection of excess power of $>6\sigma$.

Key words: cosmic background radiation – cosmology: observations – gravitational waves – inflation – polarization

1. INTRODUCTION

Precision polarimetry of the cosmic microwave background (CMB) has become a mainstay of observational cosmology. The Λ CDM model predicts a polarization of the CMB at the level of a few μ K, with a characteristic *E*-mode pattern. The *EE* power spectrum has been detected over a wide range of angular scales by many experiments, including DASI (Kovac et al. 2002), CAPMAP (Barkats et al. 2005; Bischoff et al. 2008), CBI (Readhead et al. 2004; Sievers et al. 2007), BOOMERANG03 (Montroy et al. 2006), WMAP (Page et al. 2007; Bennett et al. 2013), MAXIPOL (Wu et al. 2007), QUAD (Brown et al. 2009; Pryke et al. 2009), BICEP1 (Chiang et al. 2010; BICEP1 Collaboration et al. 2014), QUIET (QUIET Collaboration et al. 2011, 2012), POLARBEAR (POLARBEAR Collaboration et al. 2014a), BICEP2 (BICEP2 Collaboration

I 2014), ACTPol (Naess et al. 2014), SPTpol (Crites et al. 2015), and *Planck* (Planck Collaboration Results I 2014). These measurements have been in broad agreement with theoretical expectations and other cosmological data sets. Improved *EE* power spectrum data are important because they may eventually constrain the Λ CDM model parameters better than cosmic variance limited CMB temperature data (Rocha et al. 2004; Galli et al. 2014).

Of greater interest is the *B*-mode component of the polarization pattern. Though the *EE* power spectrum is higher, the *BB* power spectrum is more sensitive to new physics because the linear density perturbations at the surface of last scattering, which are the main source of *TT* and *EE* power, cannot generate *B*-mode power. On small angular scales, *BB* power instead arises from the gravitational lensing of

E -mode power by the large scale structure of the universe (Zaldarriaga & Seljak 1998). The lensing BB power thus cleanly traces the growth of structure, complementary to other methods, providing information about possible extensions to Λ CDM such as neutrino mass or a nontrivial dark energy equation of state. Measurements by SPTpol (Hanson et al. 2013), POLARBEAR (POLARBEAR Collaboration et al. 2014a, 2014b, 2014c), and BICEP2 (BICEP2 Collaboration I 2014) have provided the first evidence of BB power from gravitational lensing.

On large angular scales, lensing contributes only a small amount of BB power. However, inflationary gravitational waves (IGW) may be a source of BB power on these scales (Polnarev 1985; Kamionkowski et al. 1997; Seljak 1997; Seljak & Zaldarriaga 1997). The recent detection by BICEP2 of B -mode power on degree angular scales in excess above the lensing expectation is especially exciting because it could be evidence of primordial gravitational waves and cosmic inflation (BICEP2 Collaboration I 2014). The contribution of foregrounds to the observed BICEP2 signal is uncertain, and preliminary data from *Planck* have suggested that polarized dust in the BICEP2 field may be brighter than models had predicted (Planck Collaboration Int. XXX 2014). Regardless, a confirmation of the BICEP2 signal, whether cosmological or galactic in origin, is a top priority of observational cosmology today (Caligiuri & Kosowsky 2014; Dodelson 2014).

The Keck Array telescope is a microwave polarimeter at the South Pole designed to follow up the BICEP2 observations. The Keck Array quickly deployed a large number of detectors at 150 GHz by installing five receivers of a design very similar to BICEP2 with minimal changes. All five receivers were installed in time for the 2012 observing season and continued, with upgrades, to observe at 150 GHz through the end of 2013. The modular, multi-receiver structure of the Keck Array also allows individual receivers to be tuned to different frequencies. Two of the Keck Array receivers began observing at 95 GHz in 2014, which will help to discriminate the signal from foregrounds.

In this paper, we present the results of the 150 GHz observations by the Keck Array of the BICEP2 field during the 2012 and 2013 seasons. We begin with sections describing the Keck Array instrument, calibrations, and analysis methods. We proceed with the maps and angular power spectra obtained from this data set and perform extensive internal consistency checks. The Keck Array confirms the BICEP2 B -mode signal at $>5\sigma$. We then proceed to test for consistency between the BICEP2 and Keck Array data, and finally combine the two sets of maps to a final result.

This paper is the latest in a series of publications by the BICEP2 and Keck Array collaborations. BICEP2 Collaboration I (2014, hereafter the BICEP2 Results Paper) is directly analogous to this paper. BICEP2 Collaboration II (2014, hereafter the BICEP2 Instrument Paper) presented the full details of the BICEP2 instrument—differences are summarized in Section 2 of this paper. BICEP2 Collaboration III (2015, hereafter the Systematics Paper) presents a detailed analysis of instrumental systematics, which are treated for the Keck Array 2012–13 data in Section 7 of the current paper. Two additional papers, BICEP2/Keck Array Collaborations IV (Ade et al. 2015b, the Beams Paper) and BICEP2, Keck Array, & SPIDER Collaborations (Ade et al. 2015a, the Detectors Paper), describe the beam characterization and the detectors for both BICEP2 and the Keck Array.

2. THE KECK ARRAY INSTRUMENT

The Keck Array instrument shares much of its design with BICEP2, details of which are presented in the BICEP2 Instrument Paper. In this section, we describe the main features common to both instruments and the substantive changes and upgrades unique to the Keck Array. Figure 1 shows the receiver design for the Keck Array.

2.1. Cryostat and Cryogenic System

The Keck Array is comprised of five independent cryostats (Sheehy et al. 2010) built by Atlas Technologies.¹⁹ Inside each cryostat is a closed-cycle, three-stage ($^4\text{He}/^3\text{He}/^3\text{He}$) sorption refrigerator (Duband & Collaudin 1999) that cools the focal plane unit (FPU) to approximately 270 mK. Other optical elements are held at cryogenic temperatures to minimize the thermal load on the FPUs.

The main difference between Keck Array and BICEP2 is the bulk refrigeration system. While BICEP2 used a bath of liquid helium, the Keck Array uses a set of Cryomech²⁰ PT-410 pulse tube refrigerators. Each Keck Array cryostat has its own pulse tube refrigerator aligned along the optical axis. The helium gas is pulsed at a common frequency of 1.2 Hz, and the pressure in each system is optimized to achieve the lowest base temperature. After optimization, the pulse tubes' copper mounting surfaces typically reach 40 and 3 K with comparable performance in all five cryostats. These surfaces are thermally connected to the telescope insert by stacks of ultra high purity aluminum foil.

2.2. Optics

The Keck Array optics use an on-axis, refractive design which was originally demonstrated in the BICEP1 telescope (Takahashi et al. 2010). The entire optics chain is essentially unchanged from BICEP2 (Aikin et al. 2010). The two-lens design was chosen to accommodate the flat telecentric focal plane, with the image of the primary at infinity as viewed from the focal plane.

The lenses are made from high density polyethylene (HDPE) and cooled to 4 K. In order to sufficiently reduce the infrared loading on the cooling stages, there is a 3 mm nylon filter and two polytetrafluoroethylene (PTFE) filters of thickness 12.7 mm and 34.3 mm in the optics path, cooled to an intermediate stage of 50 K. A second nylon filter of 5.2 mm is placed between the objective and eyepiece lens, heat sunk to 4 K. A metal mesh low-pass filter (Ade et al. 2006) with a cutoff of 8.3 cm^{-1} (225 GHz) is placed above the final nylon filter to prevent any stray radiation that was not absorbed by the plastic filters from thermalizing in the detectors.

All surfaces surrounding the optical path are blackened with Eccosorb HR10²¹ cut in half and epoxied with Stycast 2850 loaded with carbon. The Stycast covers the HR10 to prevent particulate shedding during cryogenic cycling. The lining is designed such that stray light terminates on cold surfaces. Later configurations installed after the 2013 observing season included baffling on the inside of the telescope tube to further reduce reflections.

¹⁹ <http://www.atlasuhv.com/>

²⁰ <http://www.cryomech.com/>

²¹ Emerson & Cuming Microwave Products, Randolph, MA 02368. Phone: 781-961-9600. Web site: <http://eccosorb.com/>

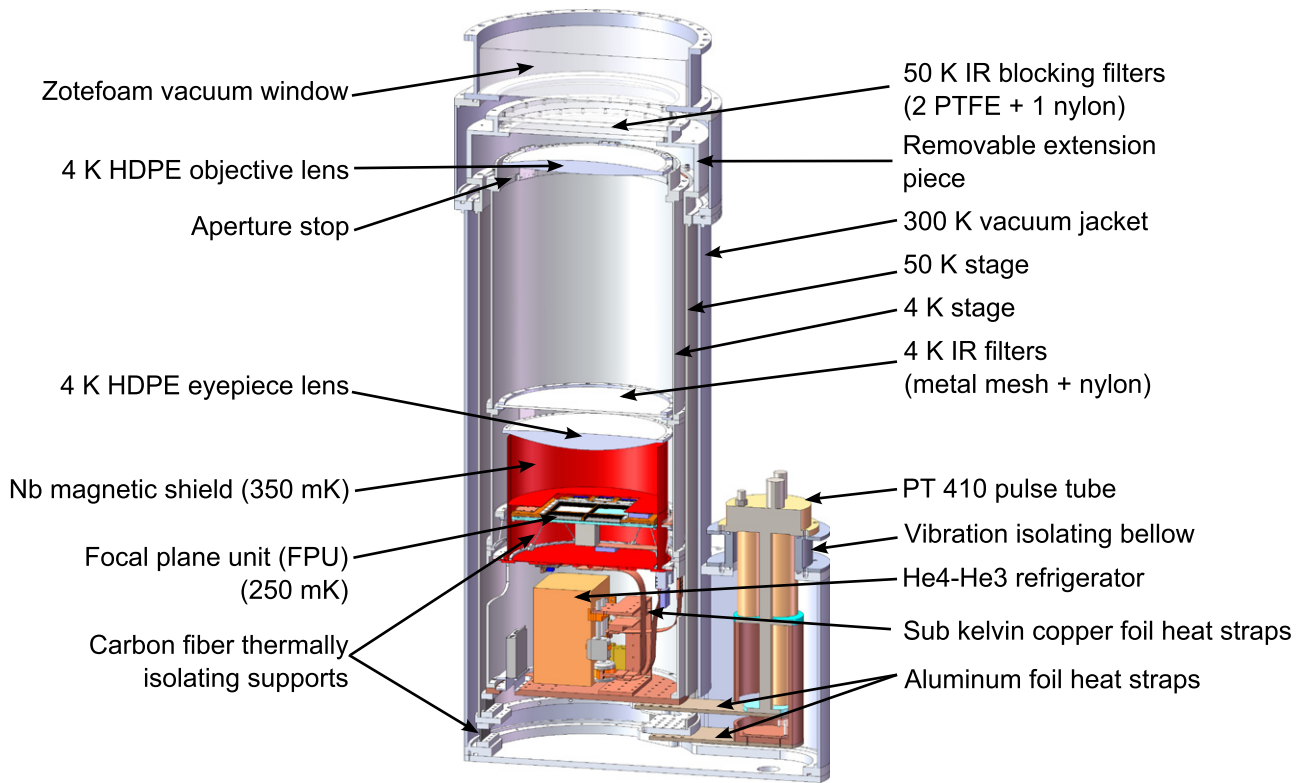


Figure 1. Individual receiver of the Keck Array. Each receiver is cryogenic, with a pulse tube refrigerator cooling the optics to 4 K and a three-stage sorption refrigerator cooling the focal plane to 270 mK. The Keck Array consists of five identical receivers on a single telescope mount at the South Pole.

The aperture stop is similarly made from a ring of 1.9 cm thick Eccosorb AN-74, beveled at 40° with an inner diameter of 26.4 cm. Approximately 20% of the total throughput is absorbed by the aperture stop. The aperture stop is placed on the lower surface of the objective lens.

2.3. FPU

The detectors, developed at Jet Propulsion Laboratory (JPL) for joint use in the BICEP2, SPIDER, and Keck Array experiments, consist of planar antennas, each an array of slot sub-antennas combined in phase, and feeding into dual series Ti and Al Transition-Edge Superconducting (TES) bolometers. A detailed description is given in the Detectors Paper. Each pixel consists of two interleaved phased antenna arrays with orthogonal polarization directions. The signal is bandpass filtered by a lithographed filter in stripline after the antenna and terminated on a thermally isolated island which also contains the series TES. A single Si tile contains 64 detector pairs and an FPU has 4 tiles. In each focal plane, eight detector pairs are left “dark.” Dark detectors consist of the complete TES island structure, but are not connected to their corresponding antennas.

The FPUs in the Keck Array were slightly modified versus those described in the BICEP2 Instrument Paper. The spacing between the tiles was increased in order to reduce the electromagnetic coupling between the pixels near the edge of the tile and the copper plate. The feed network of the antennas was also redesigned to reduce the dipole beam mismatch between the polarized pairs, significantly improving the performance versus BICEP2.

The TES detectors are voltage biased and the current is inductively coupled to time-domain multiplexing SQUIDs (de

Korte et al. 2003). The Keck Array uses the NIST developed MUX09s, which have a gradiometric design that reduces the sensitivity of the SQUIDs to uniform magnetic fields by three orders of magnitude in comparison to the MUX07a design used in BICEP2 (Stiehl et al. 2011).

After the deployment of BICEP2, we discovered that the aliased noise from the multiplexing system was affecting the overall sensitivity of the instrument. One way to mitigate the aliased noise is to increase the Nyquist inductors that limit the bandwidth of the detectors. The choice of inductance is balanced with the need for the L/R time constant to be fast enough for the detectors to be in stable negative electrothermal feedback. The first focal plane produced for the Keck Array has Nyquist chips with an inductance of $1.35 \mu\text{H}$ consistent with BICEP2, and all subsequent focal planes have an increased inductance of $2 \mu\text{H}$. This limits the bandwidth to $\leq 18 \text{ kHz}$.

2.4. Readout

The configuration of the room temperature electronics that interface with the Keck Array is similar to that described in the BICEP2 Instrument Paper. A Multi-Channel Electronics (MCE) crate provided by the University of British Columbia mounts directly to the outside of each cryostat to interface with the SQUIDs and supply the detector bias (Battistelli et al. 2008). The Keck Array MCE crates use lower power SQUID series array readout cards compared to earlier designs in order to stay compatible with a development program to improve operability on balloon-borne telescopes.

Housekeeping thermometry is read through “backpacks” attached to the cryostats similar to BICEP2, and the signals are collated and digitized in a common BLASTbus2 crate provided by the University of Toronto (Benton et al. 2014). Both the

Table 1
The Keck Array Detector Parameters

Detector Parameter	Median Value
Optical efficiency, η	24%
Band center, $\langle\nu\rangle$	151 GHz
Spectral bandwidth, $\Delta\nu$	42 GHz
Normal resistance, R_N	62 m Ω
Operating resistance, R_{op}	0.68 R_N
Saturation power, P_{sat}	9.9 pW
Optical loading, P_{opt}	3.1 pW
Thermal conductance, G_c	90 pW/K
Transition temperature, T_c	520 mK
Thermal conductance exponent, β	2.5

housekeeping and detector electronics are connected to a set of Linux-based computers and recorded to disk using the control software `gcp` at a sample rate of 20 Hz (Story et al. 2012).

2.5. Mount

All five Keck Array receivers are attached to a common telescope mount located at the Martin A. Pomerantz Observatory (MAPO) at the Amundsen–Scott South Pole Station. This mount was previously used for the DASI (Leitch et al. 2002) and QUAD (Hinderks et al. 2009) experiments. A new front end “drum” for the Keck Array cryostats was installed in 2010. The platform was leveled at that time to account for gradual shifts of the building on the snow relative to the horizon.

The mount has three axes: elevation, azimuth, and boresight. The rotation around the boresight is referred to as “deck rotation” and allows for cancellation of some systematic effects and/or tests for their presence.

3. CHARACTERIZATION

The Keck Array has been extensively characterized in laboratory tests and with in situ calibration measurements. The characterization program was very similar to the one described in Sections 10 and 11 of the BICEP2 Instrument Paper. This section summarizes these measurements, focusing particularly on detector properties that have been reoptimized since the fabrication of the BICEP2 detectors. The spectral band, optical efficiency, and bolometer thermal conductance have a strong effect on the ultimate sensitivity of the instrument, and are tuned to minimize noise while allowing stable operation under typical South Pole atmospheric loading conditions. These detector properties, summarized in Table 1, are described in Sections 3.1–3.3. We have also extensively measured the far-field beams with in situ observations of a mast-mounted source. The beam mapping measurement and its results are summarized here in Section 3.4 and described more fully in the Beams Paper.

3.1. Spectral Response

The frequency response of the antennas and lumped element filters was tuned to give a fractional bandwidth of 25%. The ~ 150 GHz observing band is bracketed by the 118.8 GHz oxygen line on the low side and the 183.3 GHz water line on the high side.

The frequency response $S(\nu)$ of the 150 GHz detectors was characterized using a Martin–Puplett Fourier transform spectrometer (FTS) (Karkare et al. 2014). From these spectra, the band

center and the bandwidth are calculated. The band center is defined to be

$$\langle\nu\rangle = \frac{\int \nu I(\nu) S(\nu) d\nu}{\int I(\nu) S(\nu) d\nu} \quad (1)$$

and the bandwidth

$$\Delta\nu = \frac{(\int I(\nu) S(\nu) d\nu)^2}{\int I^2(\nu) S^2(\nu) d\nu}, \quad (2)$$

where $I(\nu)$ is the source spectrum relative to a Rayleigh–Jeans spectrum. For a Rayleigh–Jeans spectrum, the 150 GHz detectors were measured to have a band center of 151.5 ± 1.9 GHz and a bandwidth of 41.8 ± 1.4 GHz. The effective band center shifts to 150.6, 152.8, and 148.6 GHz, respectively, for a source spectrum of CMB, dust, and synchrotron radiation using the current best-fit models (Bennett et al. 2013; Planck Collaboration Int. XXX 2014). The standard deviations are dominated by variation from tile to tile, with smaller variation from detector to detector within a tile.

3.2. Optical Efficiency

The end-to-end optical efficiency is defined as the fraction of incident light absorbed by the detectors. This is dependent on the losses in the optics, the antennas, and the bandpass filters. A higher optical efficiency increases the sensitivity of the detectors. Because it also increases the optical loading and photon noise, it must be taken into account when optimizing the thermal conductivity of the detector.

The optical efficiency is measured in the lab using a beam-filling, microwave absorbing cone of AN-72. The power change on the detector for a source in the Rayleigh–Jeans limit ($h\nu \ll kT$) is:

$$P_{opt} = kT\eta\Delta\nu \quad (3)$$

where η is the optical efficiency and $\Delta\nu$ is the bandwidth as defined in Section 3.1. The detector loading was measured with the cone at both room temperature and liquid nitrogen temperature and converted into optical efficiency with the measured bandpass of 42 GHz.

The median measured end-to-end optical efficiency of the Keck Array receivers was 24%. The optical efficiency of the early Keck Array detectors was lower than the 38% optical efficiency of the BICEP2 detectors. Detector testing after initial Keck Array deployment suggested that the optical efficiency was being reduced by microscopic stress-induced cracks in the niobium microstrips connecting the antenna networks to the TES bolometers. In later generations of Keck Array detectors the Nb film stress was decreased from ~ 1000 MPa to < 300 MPa. The optical efficiency was observed to increase as described in more detail in the Detectors Paper.

3.3. Thermal Conductance

As is discussed in the BICEP2 Instrument Paper, the detector parameters can be tuned during fabrication in order to optimize the noise performance. In particular, the thermal conductance can be tuned to minimize the phonon noise while maintaining a margin of safety ensuring operability under normal loading conditions.

The phonon noise is the thermal fluctuations from the substrate to the detector island through the SiN isolation legs. The noise-equivalent-power (NEP) is dependent on the thermal conductance G across the legs (see, e.g., Irwin & Hilton 2005) as

$$\text{NEP} = \sqrt{4k_B G T_c^2 F}, \quad (4)$$

where F is a numerical factor describing the nonlinearity of the thermal conductance between the substrate temperature and the bath temperature (typically 0.5 for these detectors).

The saturation power of the detectors is dependent on the thermal conductance as:

$$P_{\text{sat}} = G_0 T_0 \frac{(T_c/T_0)^{\beta+1} - 1}{\beta + 1} \quad (5)$$

where the exponent β is roughly 2.5 for these detectors. For the Keck Array the loading from the optics and the sky was modeled to be $\sim 22 \text{ K}_{\text{RJ}}$. The optical efficiency is used to convert the loading temperature to a power deposited on the detector. For the median optical efficiency described in Section 3.2, this corresponds to $P_{\text{opt}} = 3.1 \text{ pW}$ of loading under normal observing conditions. Assuming a safety factor of 2, the optimal G_c is then 67 pW/K .

The thermal conductance G_c was measured using detector load curves with the substrate held at different temperatures. This method used “dark” detectors that were purposefully disconnected from their antennas to avoid the optical loading effects. The detectors used in BICEP2 had higher G_c , with two tiles centered at 100 pW/K and two centered at 140 pW/K . The tiles fabricated in later runs for the Keck Array had lower thermal conductances, with a median G_c of 90 pW/K . Several tiles had a much lower G_c of $30\text{--}50 \text{ pW/K}$, expected to give lower phonon noise but a smaller margin of safety against saturation.

Finally, the margin of safety can be verified by measuring the electrical power P_J required to keep the detector in transition during standard observation. The standard observing schedule includes load curves (bolometer current-voltage measurements) taken once per hour. These have been used retrospectively to assess the safety margin under actual atmospheric conditions. With the telescope pointed at 55° in elevation, the detectors were found to have a median margin of safety of 6.8 pW , corresponding to a safety factor of 3.2.

3.4. Beams

The beam shapes were measured in situ at the South Pole by scanning on a large thermal noise source mounted $\sim 200 \text{ m}$ away, in the optical far field. All receivers in the Keck Array have a beam width of 0.22° , with very low levels of ellipticity. As in BICEP2 the dominant differential beam imperfection for the Keck Array is differential pointing. The beam mapping campaign, extracted beam parameters, and residual beam features are described in detail in the Beams Paper. In this paper we use the high-fidelity per-detector beam maps as a convolution kernel for simulations to place a limit on the false B -mode signal from beam imperfections. The simulations and results are described in Section 7.

Table 2
The Keck Array Observation Phases

Phase	LST Time	Field	Elevation (deg)	Azimuth (deg)
A	Day 0 23:00	Cryo service
B	Day 1 05:30	CMB	55.00–57.25	120–300
C	Day 1 14:30	CMB	57.50–59.75	–10–170
D	Day 1 23:00	Galaxy	55.00–56.50	130–270
E	Day 2 05:30	CMB	57.50–59.75	120–300
F	Day 2 14:30	CMB	55.00–57.25	–10–170

4. OBSERVATIONS AND DATA SET

4.1. Observations

The observation strategy of the Keck Array in the 2012 and 2013 seasons was very similar to that used by BICEP2, as described in the BICEP2 Results and Instrument Papers. The same field as BICEP2 (and BICEP1) was observed—a region centered at R.A. 0^{h} , decl. -57.5° . As viewed from the South Pole, the observing field remains at constant elevation and rotates in azimuth once per day. For fifty minute periods the telescope scanned in azimuth at a fixed elevation, forming a “scanset” with 102 half-scans. Between scansets, the azimuth was updated by approximately 12.5° to account for the sky rotation, and stepped in elevation by 0.25° . Before and after each scanset, an elevation nod was performed to calibrate the relative gain of the detectors. The scan rate in azimuth was 2.8 S^{-1} .

A group of ten scansets over successive azimuth ranges (and stepping in elevation) is called a “phase.” Table 2 shows the phases for the Keck Array. The elevation ranges were switched between phases after each full cycle of schedules. Since the briefest sub-kelvin hold time among the set of five helium sorption refrigerators was $\sim 48 \text{ hr}$, the standard observing schedule consisted of four CMB phases and one galaxy phase between fridge cycles.

As for BICEP2, the Keck Array mount allows for rotation of the whole apparatus around the line of sight—referred to as “deck rotation.” This rotation was performed between each two day schedule. For BICEP2 and the Keck Array in 2012, four deck angles were used: 68° , 113° , 248° , and 293° . These four angles provide coverage in Q and U and allow for cancellation of systematic effects whose sign reverses under 180° rotation. In 2013, the Keck Array started observing at eight deck angles: 23° , 68° , 113° , 158° , 203° , 248° , 293° , and 338° . This allows for a more complete cancellation of beam systematics—see the Systematics Paper.

4.2. Data Selection

As described in the BICEP2 Results and Instrument Papers, data cuts are applied in three distinct stages. A few cuts remove half-scans from the scansets, while a larger number cut entire scansets from the final map. The final cut stage is the channel selection cut which is applied during the final coaddition stage. These three stages provide the necessary flexibility and granularity. The cuts are summarized in Table 3 for the 2012–2013 data set (cf. Table 7 of the BICEP2 Instrument Paper).

Table 3
Data Selection Cuts for the Keck Array for 2012–2013

Cut	Total Time (10^6 s)	Integration (10^9 det-s)	Fraction Cut (%)
Before cuts	18.3	30.4	...
Channel cuts	18.3	27.5	9.5
Synchronization	18.1	27.2	1.2
Deglitching	17.8	23.6	11.8
Passing channels 1	17.6	23.3	0.58
Elnod calibration	17.1	19.9	11.2
TES fractional resistance	17.1	19.6	0.88
Time stream skewness	17.1	17.8	6.2
Time stream variance	17.0	17.4	1.2
Noise stationarity	16.9	17.0	1.4
FPU Temperature	16.7	16.7	0.84
Telescope pointing	15.7	15.8	3.0
Passing data	15.4	15.6	0.55

4.3. 2012–2013 Data Set and Sensitivity

The telescopes continuously took data through the South Pole winter. Each of 2012 and 2013 produced nearly 4500 scansets of data for a total of 18×10^6 s of data. After the data selection cuts, an average of 50% of the data remain, for a total of 15.6×10^9 det-s. This is shown graphically in the top panel of Figure 2 (Cf. Figure 23 of the BICEP2 Instrument Paper).

The instantaneous sensitivity of the Keck Array instruments is measured using two methods: by taking the average of the time stream noise spectra between 0.1 and 1 Hz and by measuring the standard deviation of the noise-only maps weighted by the square root of integration time (Kernasovskiy et al. 2012). Both methods yielded a noise-equivalent temperature (NET) of $11.5 \mu\text{K}_{\text{CMB}}\sqrt{s}$ for 2012 and $9.5 \mu\text{K}_{\text{CMB}}\sqrt{s}$ for 2013. The middle panel of Figure 2 shows the instantaneous sensitivity calculated with the time stream based method for the 2012–2013 seasons. Using the same method as described in the BICEP2 Results and Instrument Papers the map depth for the Keck Array 2012–2013 150 GHz data is 74 nK in nominal square-degree pixels ($4.4 \mu\text{K arcmin}$) over an effective area of 390 square degrees for a total sensitivity of 2.6 nK. An equivalent way of expressing the sensitivity of the data set is the survey weight $W = 1/s^2 = 150,000 \mu\text{K}^{-2}$, where s is the total sensitivity. This expression is useful because it scales linearly with integration time, number of detectors, and statistical sensitivity to r .

5. LOW LEVEL DATA REDUCTION, MAP MAKING AND SIMULATIONS

5.1. Analysis Pipeline

The Keck Array and BICEP2 data analysis uses the same code and proceeds in parallel, enabling cross checks between these independent data sets. The process used here is exactly the same as described in the BICEP2 Results Paper—a summary follows.

5.2. Low Level Reduction

As detailed in the BICEP2 Results Paper, the first step in the low level reduction is to deconvolve the temporal response of the instrument. The TES detectors have a fast response of

~ 1 ms that can be ignored. Both the MCE and the gcp apply low pass filters to the data which must be accounted for in the deconvolution.

At this stage, relative calibration is accomplished by dividing the time streams by the individual detector gains derived from elevation nods. The data are then multiplied by the median gain across the array in order to remove dependence on atmospheric variation.

5.3. Pairmaps

The sum and difference of each detector pair is taken. Each half-scan is subjected to third order polynomial filtering to remove atmospheric variation. In addition, the mean of the half-scans over the scanset is subtracted to remove any scan-synchronous contamination. The pointing of each detector pair is reconstructed from the telescope pointing model and per-pair offset angles refined by regressing per-channel maps against a WMAP5 template. At this point the time stream data of each pair are binned into a rectangular grid of pixels forming per scanset “pairmaps.” We also sample and bin the *Planck* 143 GHz temperature map and its derivatives to use in the deprojection of beam systematics. For further details see the BICEP2 Results Paper and the Systematics Paper.

5.4. Full Maps

Finally, the pairmaps are coadded into final full maps, and also into various pairs of jackknife splits. The deprojection templates are fit and removed during this process. Absolute calibration of the maps is performed by comparing the power spectrum of the temperature map with the *Planck* 143 GHz map as described in the Instrument Paper.

Figure 3 shows the resulting temperature and Stokes Q and U polarization maps for the Keck Array 150 GHz data from the 2012 to 2013 observing seasons. The left column shows the final maps and the right hand column shows a difference (jackknife) map which is consistent with noise alone. The vertical/horizontal stripes in the Q maps and the diagonal stripes in the U maps are characteristic of the E -mode polarization signal, which dominates the maps.

5.5. Simulations

We create signal and noise simulations exactly as described in the BICEP2 Results Paper. We generate realizations of noise by randomly flipping the signs of the pairmaps when co-adding to full maps. Several kinds of signal simulations are made by resampling input maps from the *synfast* program (part of the *Healpix*²² package Górski et al. 2005). The simulated data are then binned into pairmaps and combined to full maps exactly in parallel with the treatment of the real data.

6. RESULTS

6.1. Power Spectra

The maps are converted into angular power spectra exactly as described in the BICEP2 Results Paper. The matrix based purification of the Q and U maps is performed prior to inversion to form B -modes to avoid E to B mixing due to the sky-cut and filtering. A variant of the MASTER procedure

²² <http://healpix.sourceforge.net/>

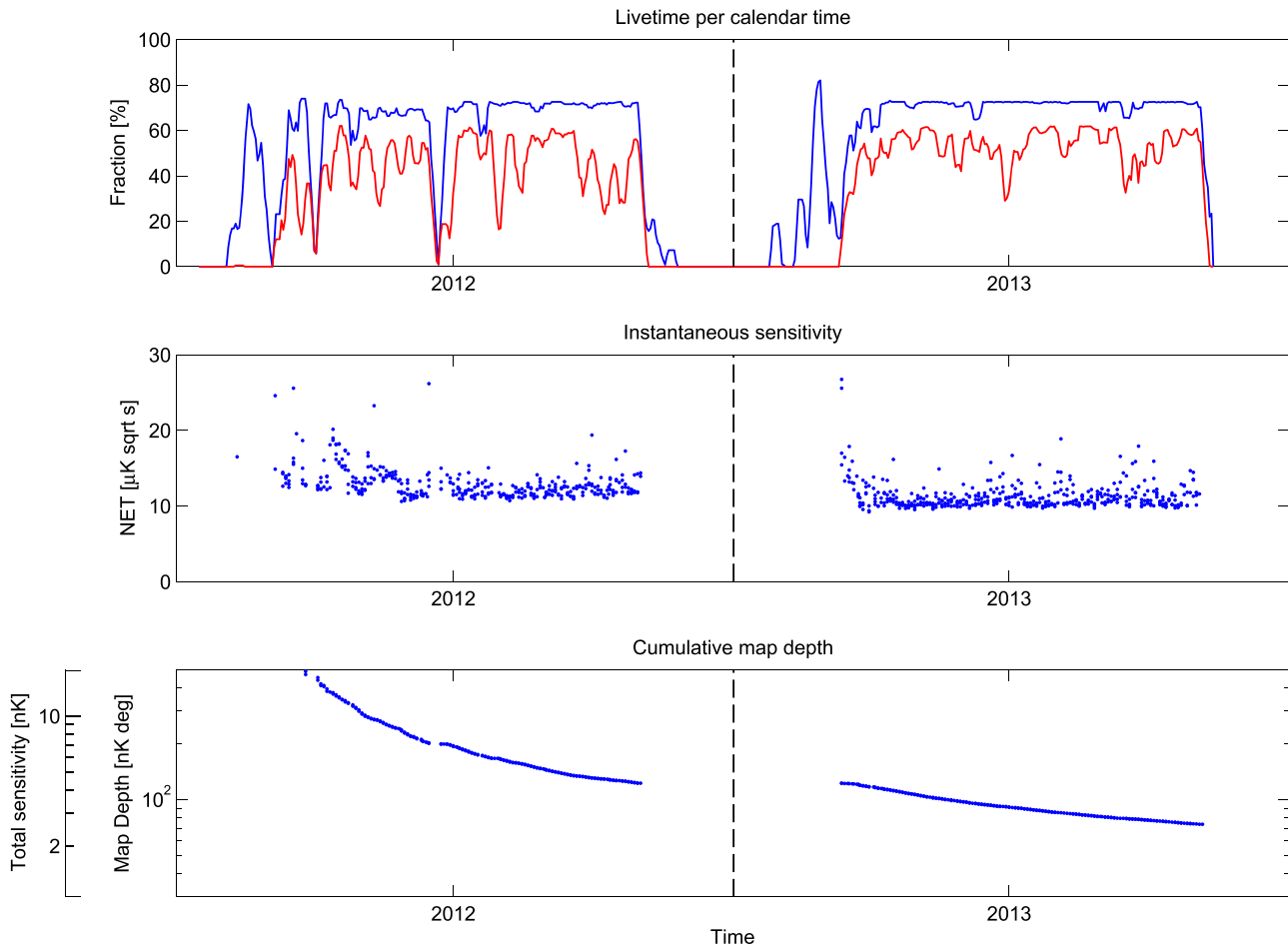


Figure 2. The Keck Array 2012–2013 150 GHz data set. The top panel shows the fraction of calendar time the telescopes were observing. The red line represents the fraction of time preserved after all data selection cuts are implemented. The middle panel shows the instantaneous sensitivity of the full Keck Array. The bottom panel shows the cumulative map depth as calculated over each phase (10 hr of data).

(Hivon et al. 2002) is used to noise debias the auto spectra and correct for the effects of the time stream filtering.

The resulting power spectra for the Keck Array using the 150 GHz data from the 2012 to 2013 observing seasons is shown in Figure 4, along with a temporal jackknife. The B -mode power spectrum is inconsistent with Λ CDM cosmology without foregrounds at 5.0σ (over the first five band powers). Although the noise is lower than for BICEP2, the first two band power values are also lower so the significance is somewhat smaller.

An overall rotation is applied to the maps to minimize the high- ℓ TB and EB spectra (Kaufman et al. 2014). For the Keck Array 2012+2013 data this adjustment is $\approx -0.5^\circ$. This rotation makes no practical difference to the B -mode power spectrum.

6.2. E and B Maps

E -mode and B -mode maps can be made by performing an inverse Fourier transform as shown in Figure 5. The maps created are inherently apodized, as the E -mode and B -mode components are generated from apodized Q and U maps. These are compared to a lensed- Λ CDM+noise simulation.

6.3. Internal Consistency Tests

The Keck Array data was split in 16 different ways to test for internal consistency. The motivations behind these splits are

described in the BICEP2 Results Paper and the Systematics Paper. If a contaminating signal exists in only one half of the data split, then it should show up with as much significance in the jackknife as in the signal map. However, some jackknives are more sensitive to certain systematics than the signal map because of inherent cancellation effects which operate in the full map. Each of the jackknife categories is summarized below.

The first set of jackknives probes for systematics which differ between different subsets of channels. This includes division in the multiplexing system, as well as divisions in the focal plane layout: tile, focal plane inner/outer, tile inner/outer, mux row, mux column. As is documented in the Beams Paper, there are systematics that are highly dependent on the position of the detector in the focal plane. For instance, the ellipticity of the beams is greater in the detectors near the outside of the focal plane than the inside.

The next set of jackknives is temporal. This includes both the longest time scale of 2012 data versus 2013 data, and the shortest timescale of left-going scans versus right-going scans. Owing to the changes between the 2012 and 2013 observing seasons, an early/late season jackknife acts as an alternative temporal split. The first is sensitive to the effects of different observing schedules and detectors changed between seasons, while the second is sensitive to detector time constants.

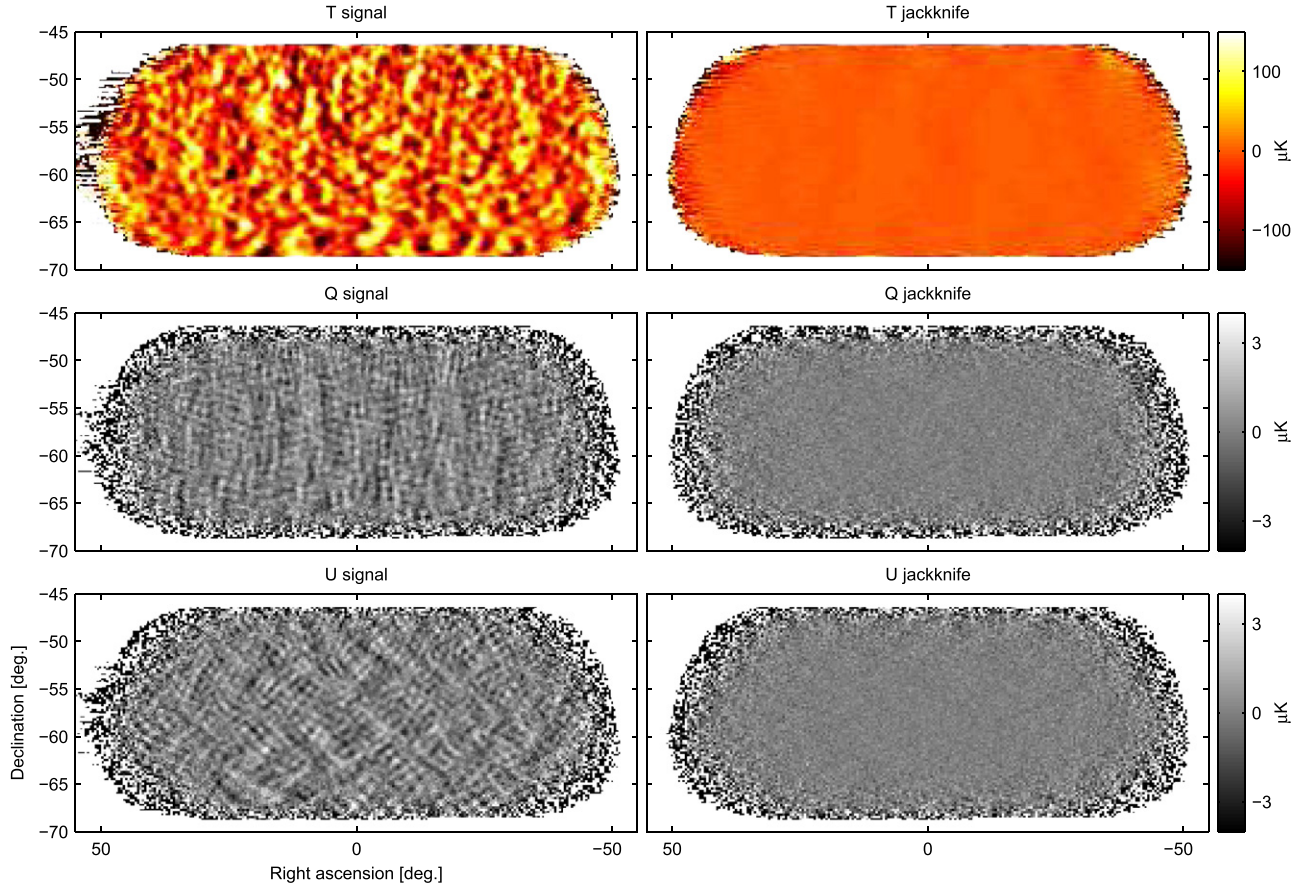


Figure 3. Keck Array T , Q , U maps. The left column shows the basic signal maps with 0.25° pixelization as output by the reduction pipeline. The right column shows difference (jackknife) maps made with the first halves of the 2012 and 2013 seasons and the second halves. No additional filtering other than that imposed by the instrument beam (FWHM 0.5°) has been done. Note that the structure seen in the Q and U signal maps is as expected for an E -mode dominated sky.

Another set of jackknives is based on external contamination. This includes the azimuth jack, which divides the data based on the direction the telescope is pointed with respect to the ground (see Table 2). One half of this jackknife is data taken in the direction of the main South Pole Station and associated operations, while the other half points into the desolate Antarctic plateau.

A set of jackknives that particularly amplifies the differential beam properties is the deck rotation jackknives. As is described in the BICEP2 Systematics Paper, a 180° deck rotation cancels out differential pointing. The deck jackknife, which differenced the 180° rotations, amplifies the leakage by an order of magnitude in comparison to that present in the fully coadded data. The Keck Array also started taking data at 90° complement deck rotations in the 2013 observing season, and this jackknife is sensitive to differential gain or differential beam width leakage. The alternative deck jackknife is defined to be the difference of the 90° rotations for 2013. In this special case, the statistics for the 2012 and 2013 data are separate.

Maps are made from each half of the data split and then differenced. The differenced maps are divided by a factor of two in order to keep the noise amplitudes equivalent to the signal map. The consistency with lensed- Λ CDM+noise simulations is calculated with a simple χ^2 statistic:

$$\chi^2 = (\mathbf{d} - \langle \mathbf{m} \rangle)^T \mathbf{D}^{-1} (\mathbf{d} - \langle \mathbf{m} \rangle) \quad (6)$$

where \mathbf{d} is the vector of observed band power values, $\langle \mathbf{m} \rangle$ is the mean of the lensed- Λ CDM+noise simulations (except where

alternative signal models are considered), and \mathbf{D} is the band power covariance matrix as evaluated from those simulations.

A χ statistic is also considered to probe for sets of band powers which are systematically above or below the expectation. This is defined as:

$$\chi = \sum_i \frac{d_i - \langle m_i \rangle}{\sigma_{m_i}} \quad (7)$$

where the d_i are the observed band power values and $\langle m_i \rangle$ and σ_{m_i} are the mean and standard deviation of the lensed- Λ CDM+noise simulations.

For each of these statistics, we calculate the probability to exceed (PTE) the observed value by comparing to the values obtained in the 500 lensed- Λ CDM+noise simulations. Since the distribution of the band powers of the auto spectra is approximately χ^2 distribution, there is some non-Gaussianity to the statistics. In particular, the lowest band power only has nine effective modes which will increase the tails of the distribution. However, by calculating the PTE against the simulations, any non-Gaussianity is fully reflected in the PTE value. The PTE for the χ and χ^2 using band powers 1–5 and 1–9 is given in Table 4. Note that these statistics are correlated (especially along each row of the table). The distribution of the PTE values is shown in Figure 6.

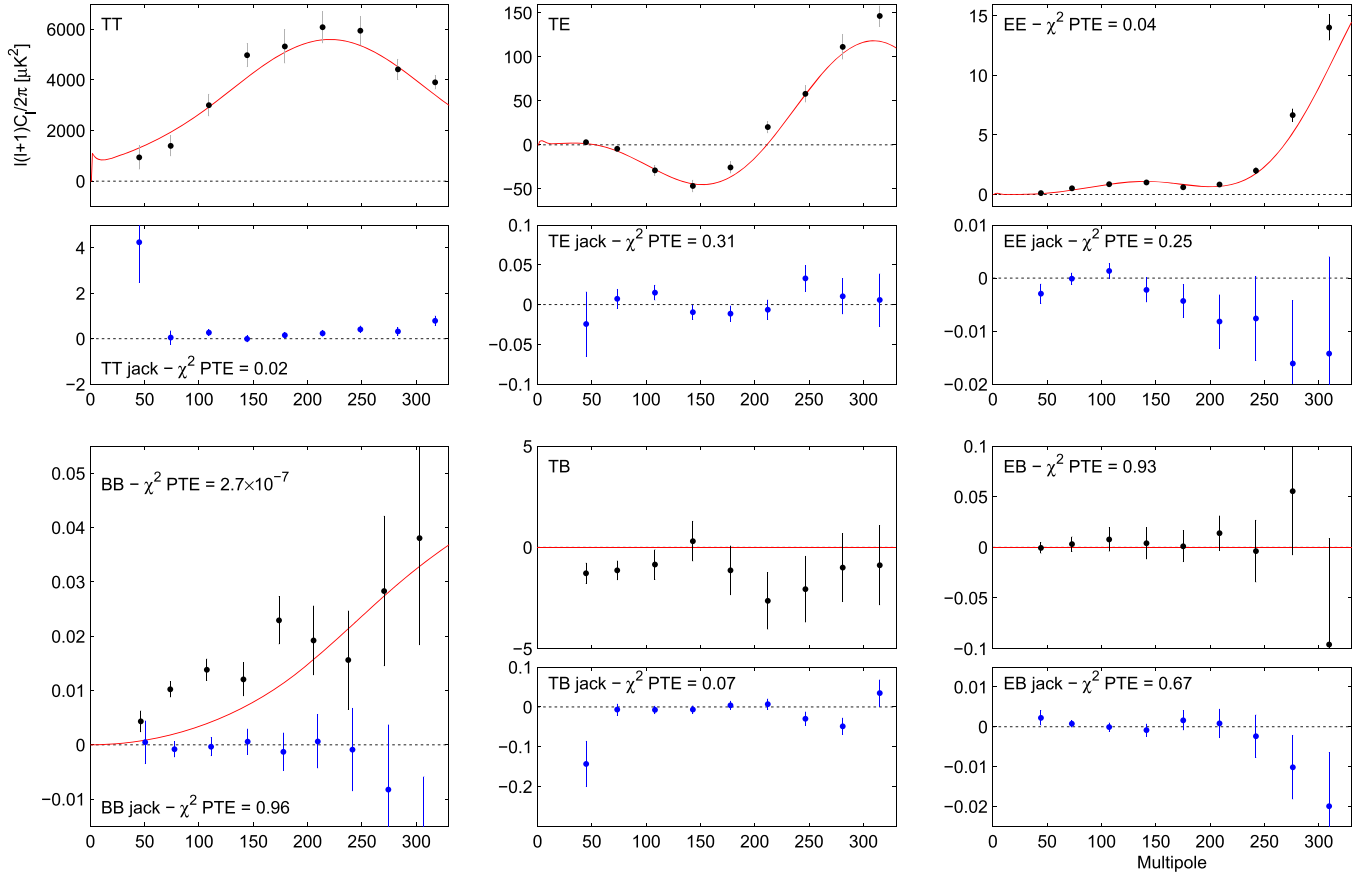


Figure 4. Keck Array power spectrum results for signal (black points) and early/late season jackknife (blue points). The solid red curves show the lensed- Λ CDM theory expectations. The error bars are the standard deviations of the lensed- Λ CDM+noise simulations and hence contain no sample variance on any additional signal component. The probability to exceed (PTE) the observed value of a simple χ^2 statistic for the 9 band powers is given (as evaluated against the simulations). Note that the band powers of the auto spectra of the simulations are approximately χ^2 distributed, with the lowest ℓ -bin only containing ~ 9 effective degrees of freedom. This increases the probability of an outlier point in comparison to a Gaussian distribution. The observed distribution for the cross spectra are more symmetric than the χ^2 distributions but have similarly increased tails. This is fully reflected in the quoted PTE value. Also note the very different y-axis scales for the jackknife spectra (other than BB). See the text for additional discussion of the BB spectrum. (Note that the calibration procedure uses EB to set the overall polarization angle so TB and EB as plotted above cannot be used to measure astrophysical polarization rotation.)

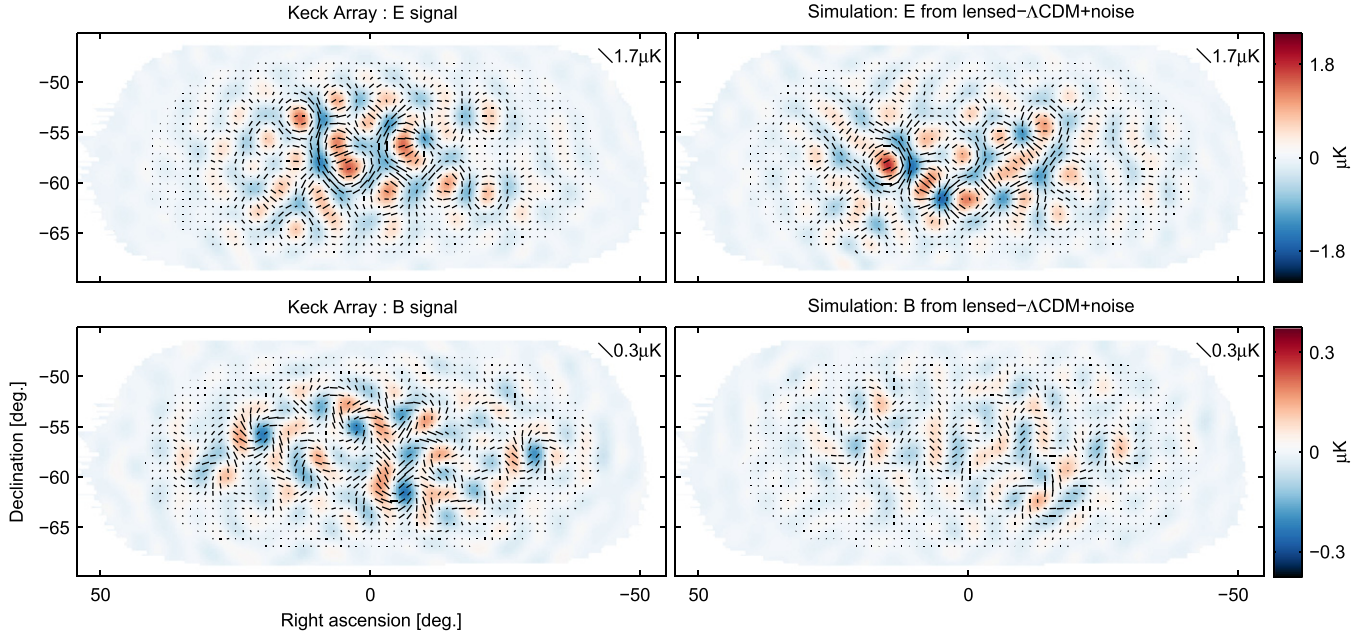


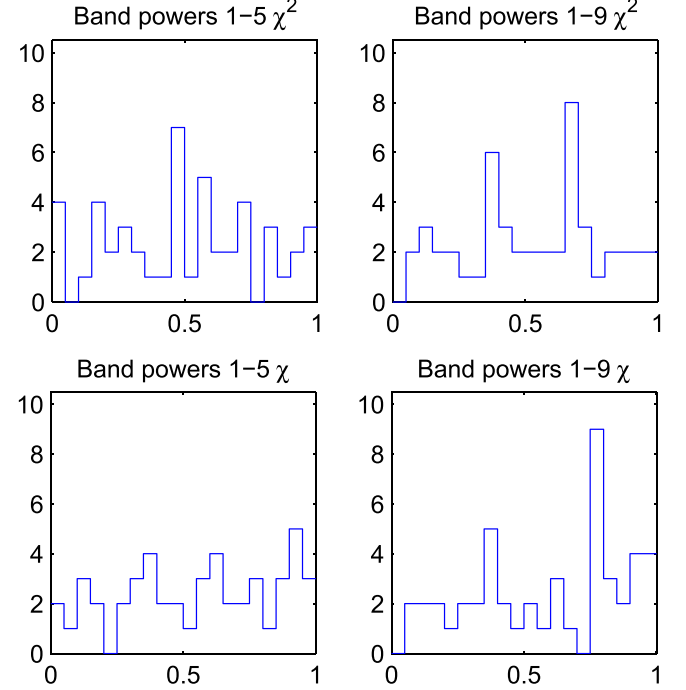
Figure 5. *Left:* Keck Array apodized E -mode and B -mode maps filtered to $50 < \ell < 120$. *Right:* the equivalent maps for the first of the lensed- Λ CDM+noise simulations. The color scale displays the E -mode scalar and B -mode pseudoscalar patterns while the lines display the equivalent magnitude and orientation of linear polarization. Note that the E -mode and B -mode maps use different color/length scales.

Table 4
Jackknife PTE Values from χ^2 and χ (Sum of Deviation) Tests

Jackknife	Band Powers 1–5 χ^2	Band Powers 1–9 χ^2	Band Powers 1–5 χ	Band Powers 1–9 χ
Deck jackknife				
EE	0.613	0.924	0.898	0.776
BB	0.743	0.880	0.685	0.375
EB	0.820	0.986	0.309	0.429
Scan Dir jackknife				
EE	0.561	0.415	0.788	0.898
BB	0.924	0.691	0.601	0.180
EB	0.168	0.453	0.938	0.886
Early/Late Season jackknife				
EE	0.287	0.255	0.896	0.998
BB	0.982	0.960	0.621	0.796
EB	0.711	0.667	0.170	0.609
Year Split jackknife				
EE	0.343	0.641	0.918	0.956
BB	0.856	0.940	0.695	0.657
EB	0.747	0.547	0.353	0.798
Tile jackknife				
EE	0.042	0.110	0.431	0.782
BB	0.573	0.715	0.118	0.499
EB	0.451	0.691	0.940	0.932
Phase jackknife				
EE	0.826	0.824	0.743	0.309
BB	0.036	0.184	0.489	0.343
EB	0.026	0.058	0.980	0.914
Mux Col jackknife				
EE	0.804	0.142	0.543	0.080
BB	0.471	0.760	0.291	0.295
EB	0.144	0.206	0.585	0.840
Alt Deck jackknife 2012				
EE	0.673	0.884	0.641	0.377
BB	0.579	0.685	0.569	0.784
EB	0.152	0.112	0.389	0.609
Alt Deck jackknife 2013				
EE	0.489	0.583	0.269	0.507
BB	0.583	0.822	0.794	0.826
EB	0.549	0.441	0.577	0.575
Mux Row jackknife				
EE	0.942	0.645	0.421	0.776
BB	0.363	0.371	0.625	0.786
EB	0.214	0.345	0.030	0.112
Tile/Deck jackknife				
EE	0.204	0.052	0.910	0.240
BB	0.487	0.745	0.986	0.830
EB	0.491	0.351	0.146	0.603
Focal Plane inner/outer jackknife				
EE	0.253	0.475	0.108	0.064
BB	0.637	0.587	0.074	0.158
EB	0.044	0.226	0.996	0.994
Tile top/bottom jackknife				
EE	0.573	0.397	0.924	0.910
BB	0.289	0.194	0.198	0.782
EB	0.172	0.353	0.884	0.954
Tile inner/outer jackknife				
EE	0.707	0.663	0.399	0.387
BB	0.303	0.663	0.719	0.786
EB	0.958	0.655	0.315	0.102
Moon jackknife				
EE	0.192	0.433	0.395	0.385
BB	1.000	0.387	0.339	0.505
EB	0.667	0.705	0.794	0.289
A/B offset best/worst				
EE	0.483	0.521	0.804	0.926
BB	0.443	0.367	0.042	0.407

Table 4
(Continued)

Jackknife	Band Powers 1–5 χ^2	Band Powers 1–9 χ^2	Band Powers 1–5 χ	Band Powers 1–9 χ
EB	0.497	0.677	0.489	0.397

**Figure 6.** Distributions of the jackknife χ^2 and χ PTE values over the tests and spectra given in Table 4.

7. SYSTEMATICS

Experimental systematics can create false B -mode polarization and must be shown to be tightly controlled. The systematics in BICEP2 were fully explored in the Systematics Paper and were shown to be below the level equivalent to $r = 0.003$ – 0.006 . These limits were derived from forward simulations of the measured instrumental properties. If a given property did not have a measured level, appropriate upper limits were used.

The beam systematics in the Keck Array are expected to be below those of BICEP2 because of the larger number of detectors (increased averaging down of incoherent effects), and the increased number of receiver orientations (both instantaneously due to the “clocking” of the five receivers at 72° increments around the boresight, and, in 2013, the increased number of deck angles of observation).

As described in the BICEP2 Results and Systematics Papers we produce simulated time streams by convolving an input temperature map with high precision per channel measurements of the actual beam shapes. We then pass these simulated time streams through the mapping process, including all filtering and deprojection, to assess the residual contamination due to beam non-ideality. The results are shown in Figure 7. The beam maps for the Keck Array do not provide as uniform and redundant coverage of all detectors as those for BICEP2 and additional analysis is required to construct composite beam maps that have consistently high signal-to-noise and are free of artifacts from the beam mapping measurement. For the

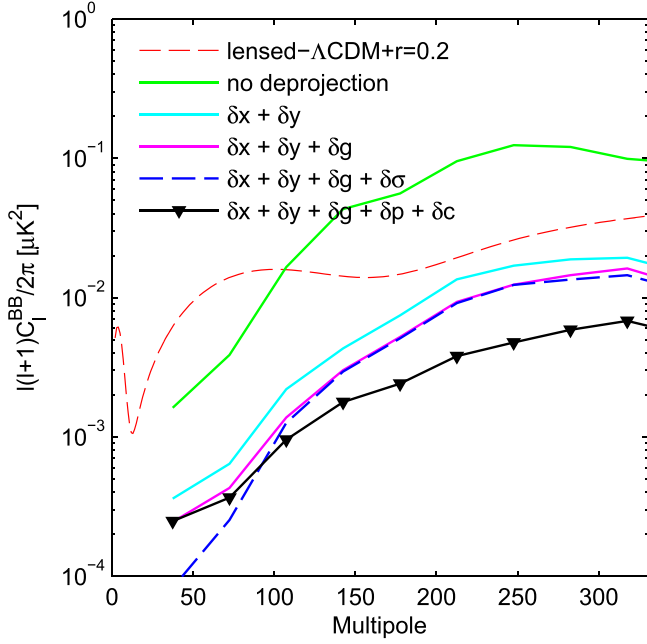


Figure 7. *BB* spectra from *T*-only input simulations using the measured per channel beam shapes compared to the lensed- Λ CDM+ $r=0.2$ spectrum. From top to bottom the curves are (i) no deprojection, (ii) deprojection of differential pointing only ($\delta x + \delta y$), (iii) deprojection of differential pointing and differential gain of the detector pairs ($\delta x + \delta y + \delta g$), (iv) adding deprojection of differential beam width ($\delta x + \delta y + \delta g + \delta \sigma$), and (v) differential pointing, differential gain, and differential ellipticity ($\delta x + \delta y + \delta g + \delta p + \delta c$). This last curve represents an upper limit only to the residual contamination.

purposes of the current paper we use the preliminary beam map results to set an upper limit on the residual contamination, as indicated by the down arrows in the figure.

Other forms of systematic contamination were considered, such as electromagnetic interference contamination, magnetic pickup, thermal pickup, and detector pointing. Each of these systematics was quantified to be below the BICEP2 level when averaged over the entire array, and thus safely ignorable.

8. CONSISTENCY WITH BICEP2

The resulting *B*-mode power spectra of BICEP2 and the Keck Array can be compared to assess the compatibility of the two sets of results. Although there is much that the two experiments share in terms of hardware, design, and location, there are also potential systematics that are different: the bulk refrigeration system, the ground shield, and the time at which the observations occurred. Comparing the results is a powerful additional systematics check. The power spectra for both the Keck Array, BICEP2 and the cross between the two are shown in the upper panel of Figure 8.

A rigorous comparison can be done in two ways: directly comparing the maps and comparing the auto and cross power spectra. The latter can be a more powerful comparison if the maps have different noise levels—since BICEP2 and the Keck Array have comparable noise levels, all four methods (map and the three combinations of auto and cross spectra) have approximately equal statistical power.

To test the compatibility of the resulting band powers with null we compare them to the differences of signal+noise simulations which share common input skies. In such tests it is necessary that the simulations contain power roughly equal to

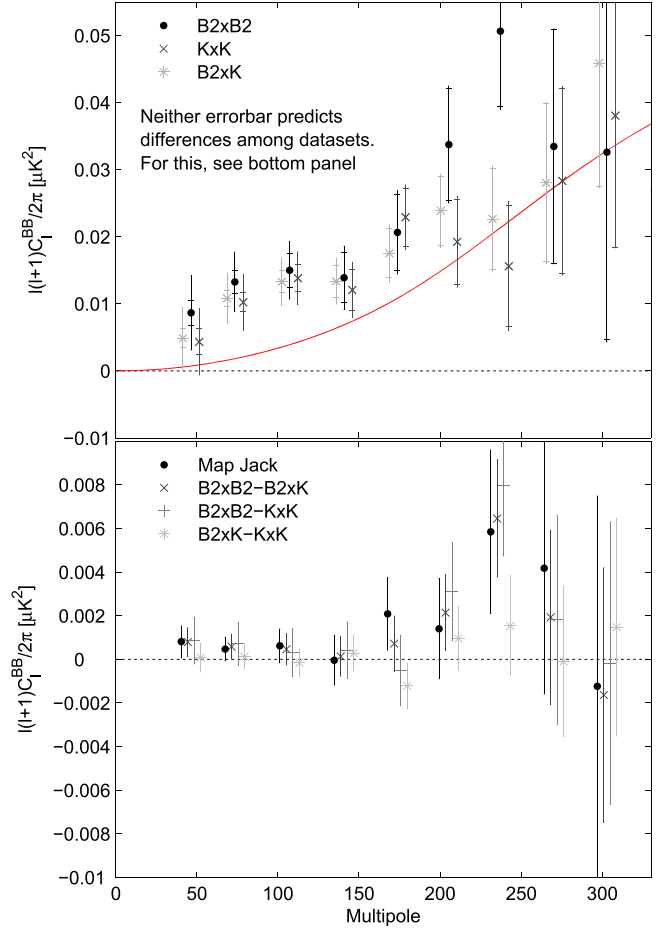


Figure 8. *Upper:* the Keck Array *BB* auto spectrum, the BICEP2 auto spectrum, and the cross spectrum taken between the two. The inner error bars are the standard deviation of the lensed- Λ CDM+noise simulations, while the outer error bars also contain excess power at low- ℓ . (For clarity the Keck Array and cross spectrum points are offset horizontally.) *Lower:* four compatibility tests between the *B*-modes measured by BICEP2 and Keck Array. The “map jack” takes the difference of the *Q* and *U* maps, divides by a factor of two, and calculates the *BB* spectrum. The other three sets of points are the differences of the spectra shown in the upper panel divided by a factor of four. In each case the error bars are the standard deviation of the pairwise differences of signal+noise simulations which share common input skies. Comparison of any one of these sets of points with null is an appropriate test of the compatibility of the experiments—see text for details. All tests show good consistency between BICEP2 and Keck Array, particularly in the lowest five bandpowers.

the real sky as the cross terms between signal and noise increase the fluctuation of the differences even for perfectly common sky coverage. For example, the (un-debiased) auto spectrum of a map *M* composed of a signal *S* and noise *N* can be written

$$M \times M = (S + N) \times (S + N) = S \times S + 2(S \times N) + N \times N. \quad (8)$$

The difference of such auto spectra between experiments with common sky coverage is then

$$M_1 \times M_1 - M_2 \times M_2 = 2(S \times N_1 - S \times N_2) + N_1 \times N_1 - N_2 \times N_2 \quad (9)$$

where M_1 and M_2 refer to the first and second experiment. The signal auto spectrum $S \times S$ cancels out. However, the cross terms between the signal and noise $2(S \times N_1 - S \times N_2)$ do

Table 5BICEP2/Keck Array Compatibility Test PTE Values from χ^2 and χ (Sum of Deviation) Tests

Jackknife	Band Powers 1–5 χ^2	Band Powers 1–9 χ^2	Band Powers 1–5 χ	Band Powers 1–9 χ
Map jackknife				
<i>EE</i>	0.034	0.048	0.106	0.028
<i>BB</i>	0.561	0.695	0.054	0.018
<i>EB</i>	0.741	0.754	0.405	0.651
Spectral jackknife B2-cross				
<i>EE</i>	0.112	0.092	0.068	0.078
<i>BB</i>	0.687	0.387	0.052	0.008
<i>EB</i>	0.555	0.224	0.212	0.234
Spectral jackknife B2-Keck				
<i>EE</i>	0.138	0.128	0.066	0.126
<i>BB</i>	0.920	0.485	0.200	0.022
<i>EB</i>	0.511	0.214	0.210	0.200
Spectral jackknife cross-Keck				
<i>EE</i>	0.176	0.204	0.074	0.202
<i>BB</i>	0.880	0.966	0.643	0.435
<i>EB</i>	0.361	0.437	0.443	0.188

not cancel, and they increase the fluctuations between the two experiments over the noise-only case in proportion to the common signal. To account for this extra variance, we use signal simulations with additional power that matches the amplitude of the observed signal in excess of Λ CDM in band powers 1–5. (The origin of the extra signal over Λ CDM is not important here—only its approximate amplitude.) The results are shown in Figure 8.

We then proceed to calculate the PTE of the χ and χ^2 statistics versus the simulated distributions using the same spectra and band power ranges as in Section 6.3, and give the results in Table 5. In both the figure and the table we note the effect of the two band powers at $\ell \approx 220$ that are high with respect to lensed- Λ CDM in B2xB2 (as noted in the BICEP2 Results Paper) but not in KxK and B2xK—as expected these also show up in the map difference. Again note that the PTE values are correlated (both along and between rows of the table) so overinterpretation should be avoided. Our conclusion is that the BICEP2 and Keck Array data are consistent—especially in the lowest five band powers where an IGW contribution would be strongest.

9. COMBINATION WITH BICEP2

Having shown that the Keck Array results are consistent with BICEP2 we now proceed to combine the maps by adding the accumulation quantities (equivalent to a noise weighted combination of the maps). This results in Q and U maps which have a depth of 57 nK deg (3.4 μ K arcmin) over an effective area of 400 square degrees. Following Section 4.3, the map depth and effective area are combined for a total sensitivity of 2.0 nK and a total survey weight of 250,000 μ K $^{-2}$.

The observation regions and strategies are sufficiently similar that it is found empirically using simulations that the purification matrix of either experiment delivers adequate B -mode purity when applied to the combined map (with contamination equivalent to $r < 10^{-3}$).

The final BB spectrum is shown in Figure 9 and is inconsistent with the lensed- Λ CDM expectation at $>6\sigma$ (for

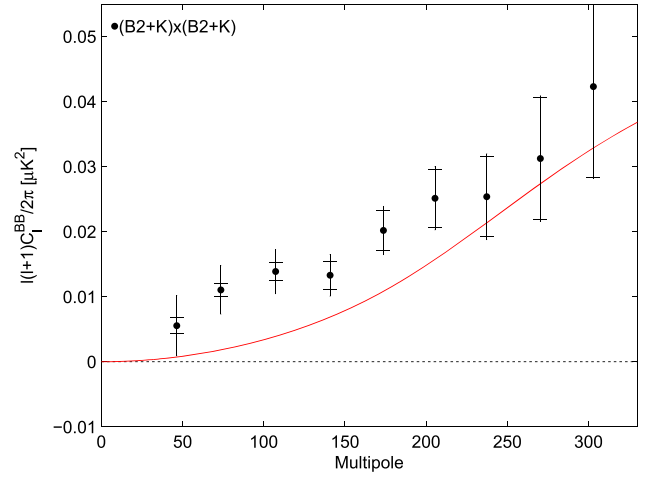


Figure 9. The BB power spectrum of combined BICEP2 and Keck Array maps. The inner error bars are the standard deviation of the lensed- Λ CDM+noise simulations, while the outer error bars also contain excess power at low- ℓ .

either band powers 1–5 or 1–9). The lensed- Λ CDM+noise error bars as plotted are approximately a factor two smaller than those of the previous BICEP2 only results—saturation on the (small) sample variance of the lensing component is occurring—the noise component is a factor 2.3 times smaller. All the spectra (including TT , EE etc.) are available for download at <http://bicepkeck.org/> together with the ancillary data, noise information etc., required to use them.

10. CONCLUSIONS

We have presented the Keck Array instrument and the 2012–2013 (150 GHz) data set. The instantaneous instrumental sensitivity of 9.5 μ K $_{\text{CMB}}\sqrt{s}$ is the best reported to date. The same area of sky as previously observed by BICEP2 was mapped to a depth in Q and U of 74 nK deg (4.4 μ K arcmin). The resulting Keck Array power spectra are consistent with lensed- Λ CDM except for an excess at degree angular scales in BB which has a significance of 5.0σ . Extensive jackknife tests argue against a systematic origin for the signal, and further statistical tests indicate that the maps and spectra are consistent with the previous BICEP2 results. Finally the two sets of maps are combined to produce maps with noise of 57 nK deg (3.4 μ K arcmin) over an effective area of 400 deg 2 for a survey weight of 250,000 μ K $^{-2}$. The final BB spectrum is inconsistent with lensed- Λ CDM at a significance of $>6\sigma$. The combined map results (for all spectra) are available for download. There does not appear to be any reason to consider the BICEP2 results as more reliable than the Keck Array results or vice versa. We therefore emphasize that we regard the combined results as the best available data set at this time.

The origin of the excess power shown in Figure 9, and previously reported in the BICEP2 Results Paper, has been extensively debated in the literature (Flauger et al. 2014; Fuskeland et al. 2014; Mortonson & Seljak 2014). Recently, concrete information on the strength of polarized dust emission at high galactic latitude has become available in Planck Collaboration Int. XXX (2014). It appears that dust emission is a significant contribution to the signal observed by BICEP2 and the Keck Array. Therefore, in an upcoming paper, the BICEP2 and combined maps are cross correlated with Planck maps of

the same region to constrain the dust contribution to the observed signal.

During the 2014 season, two of the Keck Array receivers operated at 95 GHz and a future analysis will use this data to further constrain the dust contribution. In the 2015 season BICEP3 will provide increased sensitivity at 95 GHz and operation of Keck Array receivers at 220 GHz is also planned.

The Keck Array project has been made possible through support from the National Science Foundation under Grants ANT-1145172 (Harvard), ANT-1145143 (Minnesota) & ANT-1145248 (Stanford), and from the Keck Foundation (Caltech). The development of antenna-coupled detector technology was supported by the JPL Research and Technology Development Fund and Grants No. 06-ARPA206-0040 and 10-SAT10-0017 from the NASA APRA and SAT programs. The development and testing of focal planes were supported by the Gordon and Betty Moore Foundation at Caltech. Readout electronics were supported by a Canada Foundation for Innovation grant to UBC. The computations in this paper were run on the Odyssey cluster supported by the FAS Science Division Research Computing Group at Harvard University. The analysis effort at Stanford and SLAC is partially supported by the U.S. Department of Energy Office of Science. We thank the staff of the U.S. Antarctic Program and in particular the South Pole Station without whose help this research would not have been possible. Most special thanks go to our heroic winter-overs Robert Schwarz and Steffen Richter. We thank all those who have contributed past efforts to the BICEP–Keck Array series of experiments, including the BICEP1 team.

REFERENCES

- Ade, P. A. R., Pisano, G., Tucker, C., & Weaver, S. 2006, *Proc. SPIE*, **6275**, 62750U
- Ade, P. A. R., Aikin, R. W., Amiri, M., et al. 2015a, arXiv:1502.00619
- Ade, P. A. R., Aikin, R. W., Barkats, D., et al. 2015b, *ApJ*, **806**, 206
- Aikin, R. W., Ade, P. A., Benton, S., et al. 2010, *Proc. SPIE*, **7741**, 77410V
- Barkats, D., Bischoff, C., Farese, P., et al. 2005, *ApJL*, **619**, L127
- Battistelli, E. S., Amiri, M., Burger, B., et al. 2008, *JLTP*, **151**, 908
- Bennett, C. L., Larson, D., Weiland, J. L., et al. 2013, *ApJS*, **208**, 20
- Benton, S. J., Ade, P. A., Amiri, M., et al. 2014, *Proc. SPIE*, **9145**, 94150V
- BICEP1 Collaboration, Barkats, D., Aikin, R., et al. 2014, *ApJ*, **783**, 67
- BICEP2 Collaboration I, 2014, *PhRvL*, **112**, 241101
- BICEP2 Collaboration II, 2014, *ApJ*, **792**, 62
- BICEP2 Collaboration III, 2015, arXiv:1502.00608
- Bischoff, C., Hyatt, L., McMahon, J. J., et al. 2008, *ApJ*, **684**, 771
- Brown, M. L., Ade, P., Bock, J., et al. 2009, *ApJ*, **705**, 978
- Caligiuri, J., & Kosowsky, A. 2014, *PhRvL*, **112**, 191302
- Chiang, H. C., Ade, P. A. R., Barkats, D., et al. 2010, *ApJ*, **711**, 1123
- Crites, A. T., Henning, J. W., Ade, P. A. R., et al. 2015, *ApJ*, **805**, 36
- de Korte, P. A. J., Beyer, J., Deiker, S., et al. 2003, *RSci*, **74**, 3807
- Dodelson, S. 2014, *PhRvL*, **112**, 191301
- Duband, L., & Collaudin, B. 1999, *Cryo*, **39**, 659
- Flauger, R., Hill, J. C., & Spergel, D. N. 2014, *JCAP*, **8**, 39
- Fuskeland, U., Wehus, I. K., Eriksen, H. K., & Naess, S. K. 2014, *ApJ*, **790**, 104
- Galli, S., Benabed, K., Bouchet, F., et al. 2014, *PhRvD*, **90**, 063504
- Górski, K. M., Hivon, E., Banday, A. J., et al. 2005, *ApJ*, **622**, 759
- Hanson, D., Hoover, S., Crites, A., et al. 2013, *PhRvL*, **111**, 141301
- Hinderks, J. R., Ade, P., Bock, J., et al. 2009, *ApJ*, **692**, 1221
- Hivon, E., Górski, K. M., Netterfield, C. B., et al. 2002, *ApJ*, **567**, 2
- Irwin, K., & Hilton, G. 2005, in *Cryogenic Particle Detection*, Vol. 99, ed. C. Enss (Berlin: Springer), 63
- Kamionkowski, M., Kosowsky, A., & Stebbins, A. 1997, *PhRvL*, **78**, 2058
- Karkare, K. S., Ade, P. A. R., Ahmed, Z., et al. 2014, *Proc. SPIE*, **9153**, 91533B
- Kaufman, J. P., Miller, N. J., Shimon, M., et al. 2014, *PhRvD*, **89**, 062006
- Kernasovskiy, S., Ade, Aikin, et al. 2012, *Proc. SPIE*, **8452**, 84521B
- Kovac, J. M., Leitch, E. M., Pryke, C., et al. 2002, *Natur*, **420**, 772
- Leitch, E. M., Kovac, J. M., Pryke, C., et al. 2002, *Natur*, **420**, 763
- Montroy, T. E., Ade, P. A. R., Bock, J. J., et al. 2006, *ApJ*, **647**, 813
- Mortonson, M. J., & Seljak, U. 2014, *JCAP*, **10**, 35
- Naess, S., Hasselfield, M., McMahon, J., et al. 2014, *JCAP*, **10**, 7
- Page, L., Hinshaw, G., Komatsu, E., et al. 2007, *ApJS*, **170**, 335
- Planck Collaboration Int. XXX, 2014, A&A, arXiv:1409.5738
- Planck Collaboration Results I, 2014, *A&A*, **571**, A1
- POLARBEAR Collaboration, Ade, P. A. R., Akiba, Y., et al. 2014a, *ApJ*, **794**, 171
- POLARBEAR Collaboration, Ade, P. A. R., Akiba, Y., et al. 2014b, *PhRvL*, **112**, 131302
- POLARBEAR Collaboration, Ade, P. A. R., Akiba, Y., et al. 2014c, *PhRvL*, **113**, 021301
- Polnarev, A. G. 1985, *SvA*, **29**, 607
- Pryke, C., Ade, P., Bock, J., et al. 2009, *ApJ*, **692**, 1247
- QUIET Collaboration, Araujo, D., Bischoff, C., et al. 2012, *ApJ*, **760**, 145
- QUIET Collaboration, Bischoff, C., Brizius, A., et al. 2011, *ApJ*, **741**, 111
- Readhead, A. C. S., Myers, S. T., Pearson, T. J., et al. 2004, *Sci*, **306**, 836
- Rocha, G., Trotta, R., Martins, C. J. A. P., et al. 2004, *MNRAS*, **352**, 20
- Seljak, U. 1997, *ApJ*, **482**, 6
- Seljak, U., & Zaldarriaga, M. 1997, *PhRvL*, **78**, 2054
- Sheehy, C. D., et al. 2010, *Proc. SPIE*, **7741**, 77411R
- Sievers, J. L., Achermann, C., Bond, J. R., et al. 2007, *ApJ*, **660**, 976
- Stiehl, G., Cho, H.-M., Hilton, G., et al. 2011, *ITAS*, **21**, 298
- Story, K., Leitch, E., Ade, P., et al. 2012, *Proc. SPIE*, **8451**, 84510T
- Takahashi, Y. D., Ade, P. A. R., Barkats, D., et al. 2010, *ApJ*, **711**, 1141
- Wu, J. H. P., Zuntz, J., Abroe, M. E., et al. 2007, *ApJ*, **665**, 55
- Zaldarriaga, M., & Seljak, U. 1998, *PhRvD*, **58**, 023003